Supplemental Information for:

Estimating Gas-Particle Partitioning in Mixed Emissions of Plastic and Biomass Burning Pyrolysis Products

Emily Halpern[1], Dominick Dotson[1], Qiaorong Xie[1], Peter Christ[1], Killian MacFeely[1], Lauren Heirty[1], Sergey A. Nizkorodov,[3] Alexander Laskin[1,2]

[1]*Department of Chemistry, Purdue University, West Lafayette, IN, 47907, USA.*

[2]*Department of Earth Atmospheric and Planetary Sciences, Purdue University, West Lafayette, IN, 47907, USA.*

[3]*Department of Chemistry, University of California, Irvine, Irvine, CA, 92697, USA.*

Table of Contents:

Supplemental Note 1. Chemical Characterization of Plastic Thermal Decomposition Products.

Figures S1–S5 provide a summary of TPD-DART-HRMS experimental total ion thermograms, along with the molecular characteristics of thermal decomposition products identified for four plastic types: polypropylene (PP), polyethylene (PE), polystyrene (PS), and polyvinyl chloride (PVC).

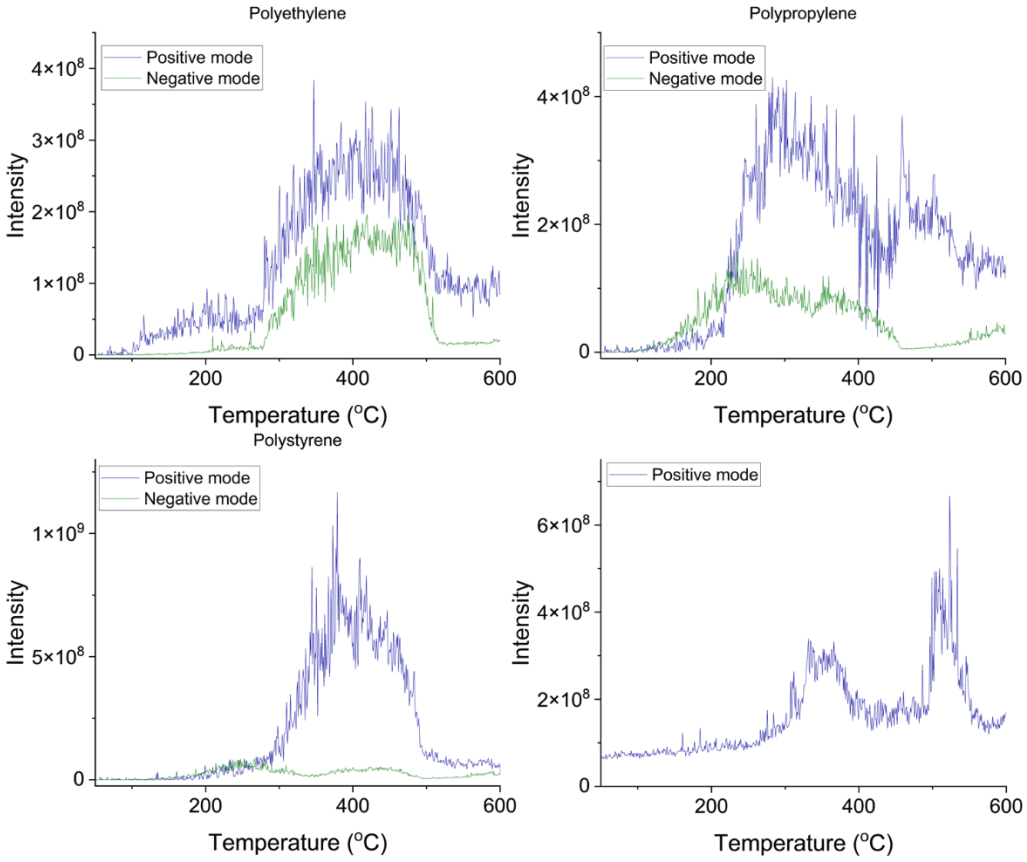

Figure S1. Total ion thermograms of positive and negative ions recorded in TPD-DART-HRMS experiments with PE, PP, PS, and PVC samples. For all plastic samples, the total ion current is higher in positive mode at most desorption temperatures. Negative ions recorded in the PVC experiments are exclusively $Cu_xCl_{x+1}^-$ clusters (Halpern et al. 2025), which are not included in this figure.

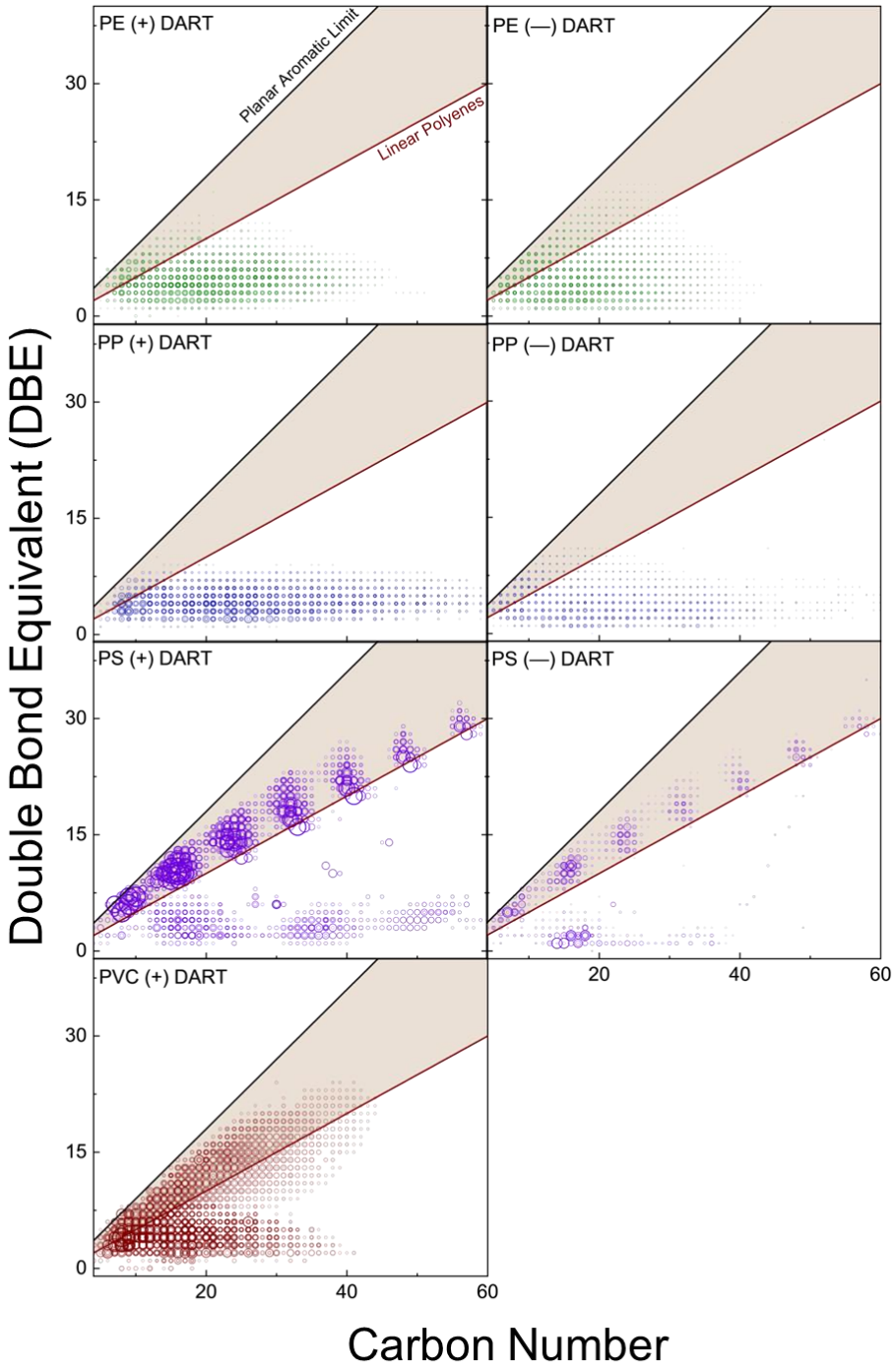

Figure S2. DBE values of plastic thermal decomposition products detected by TPD-DART-HRMS in positive (left) and negative (right) ionization modes for four plastic types, PP, PE, PS, and PVC, plotted versus carbon number, scaled to $(\text{intensity})^{1/4}$. The lines depicted in each plot planar aromatic limit (black) and linear polyenes (red) represent the limit of aromaticity for organic molecules and the line of linear polyenes, between which molecules are likely to be light absorbing. DBE values that fall within the shaded area are potentially light-absorbing; PS and PVC are likely to produce light-absorbing species when thermally decomposed.

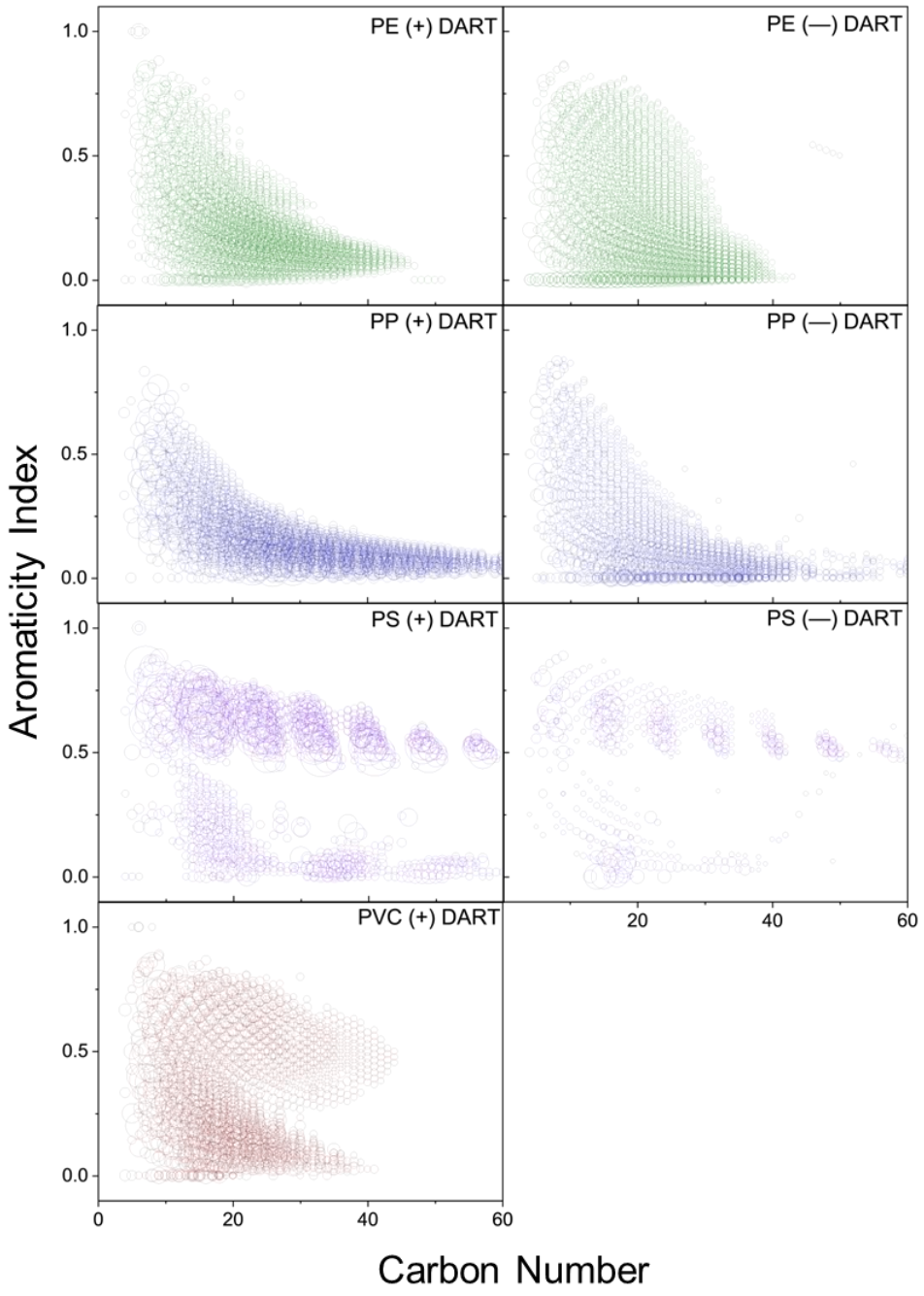

Figure S3. Aromaticity index (AI_{mod}) values of plastic thermal decomposition products detected by TPD-DART-HRMS in positive (left) and negative (right) ionization modes for four plastic types: PP, PE, PS, and PVC, plotted as a function of carbon number, scaled to $(intensity)^{1/4}$. PS and PVC produce substantial fractions of highly aromatic species ($AI_{mod} > 0.67$) with extended carbon chains (up to 40–60 carbon atoms). Aromatic products from PE and PP are less abundant and generally contain fewer than 20 carbon atoms. Across all four plastics, a significant proportion of products are highly aliphatic ($AI_{mod} < 0.2$).

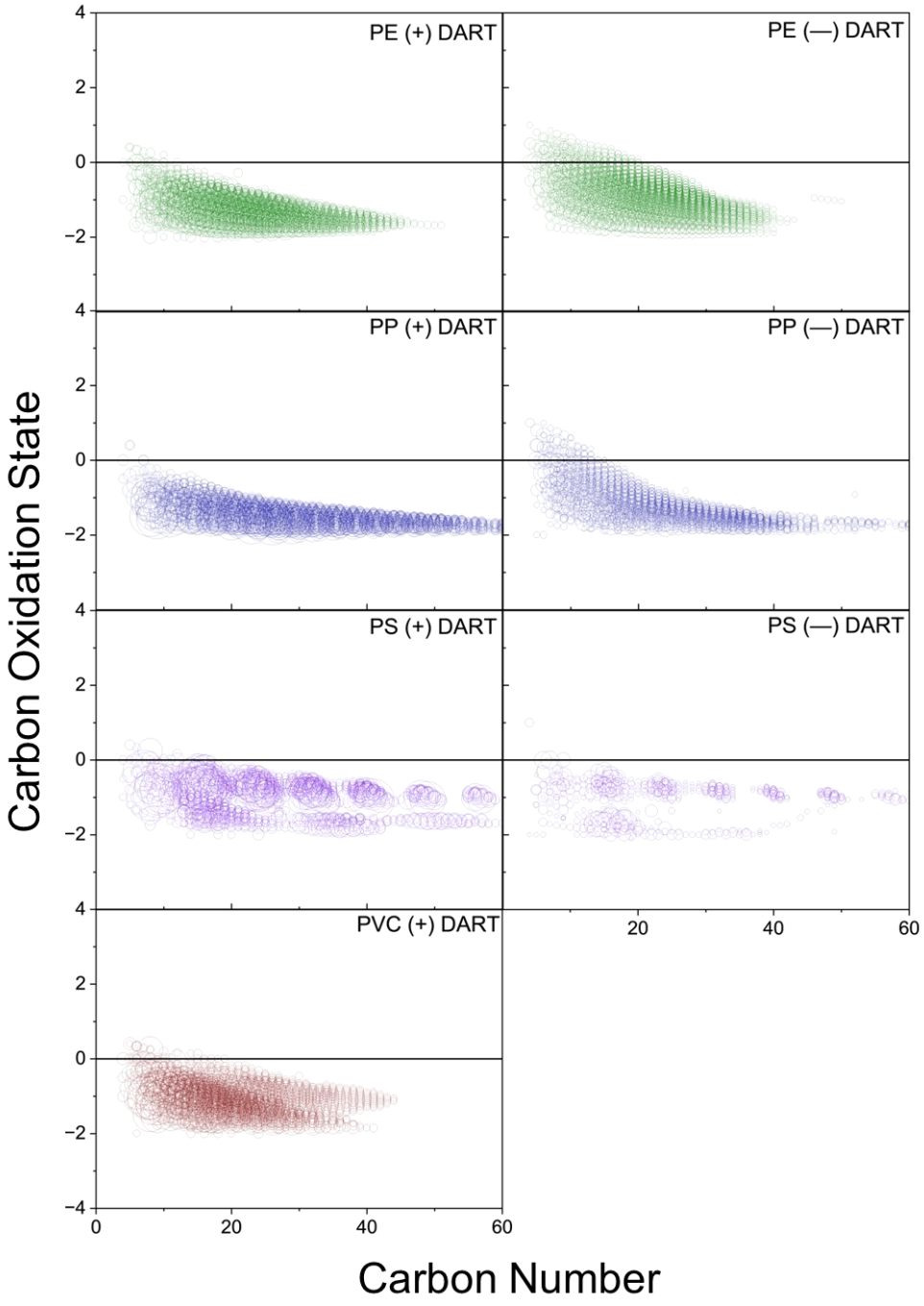

Figure S4. Carbon oxidation state (OS_c) of plastic thermal decomposition products detected by TPD-DART-HRMS in positive (left) and negative (right) ionization modes for four plastic types: PP, PE, PS, and PVC, plotted as a function of carbon number, scaled to $(\text{intensity})^{1/4}$. Most species of plastic thermal decomposition products are reduced ($OS_c<0$).

Supplemental Note 2. Estimation of Sensitivity Factors to Correct for Ionization Efficiency Variations in Polymer Pyrolysis Products.

Figure S5 depicts the geometrically optimized structures for representative thermal decomposition products of PE, PP, PS, and PVC used to determine R=CCS_{MWi}/CCS_{100} ratios. Representative species for each plastic type were selected from the most prominent homologous series identified among the detected thermal decomposition products for each polymer, summarized in Table S1. For PE, PP, and PS, the selected representative species consist of repeating units derived from their respective monomer structures, reflecting the progression of homologous series observed in their thermal decomposition products. In contrast, thermal decomposition of PVC involves rapid dehydrochlorination of the polymer backbone, leading to the formation of conjugated polyene fragments (Yu et al. 2016). Accordingly, representative polyene species were selected to characterize the thermal degradation products of PVC.

Geometrical optimization of molecular structures was performed using the Q-Chem 5 software package (Epifanovsky et al. 2021), employing density functional theory (DFT) with the B3LYP functional and the 6-31G* basis set. Collision cross sections (CCS) for each species were calculated using the Ion Mobility Spectrometry Suite (IMoS; https://www.imospedia.com/imos/) employing the projected area approximation. Mulliken partial atomic charges were also computed for the optimized molecular structures. The resulting CCS values were summarized as dimensionless ratios R=CCS_{MWi}/CCS_{100} versus MW datasets, where CCS_{100} is the reference value derived from a linear regression fit to the dataset ($R=a\times MW+b$) normalized such that R_{100}=1 (Figure S6). Due to the similarity in CCS trends observed for PE, PP, and PVC products, a single linear regression fit was applied to their data:

$$R=0.0079\times MW+0.094$$

In contrast, a separate linear fit was used for polystyrene (PS) products, reflecting their distinct structural features:

$$R=0.0041\times MW+0.592$$

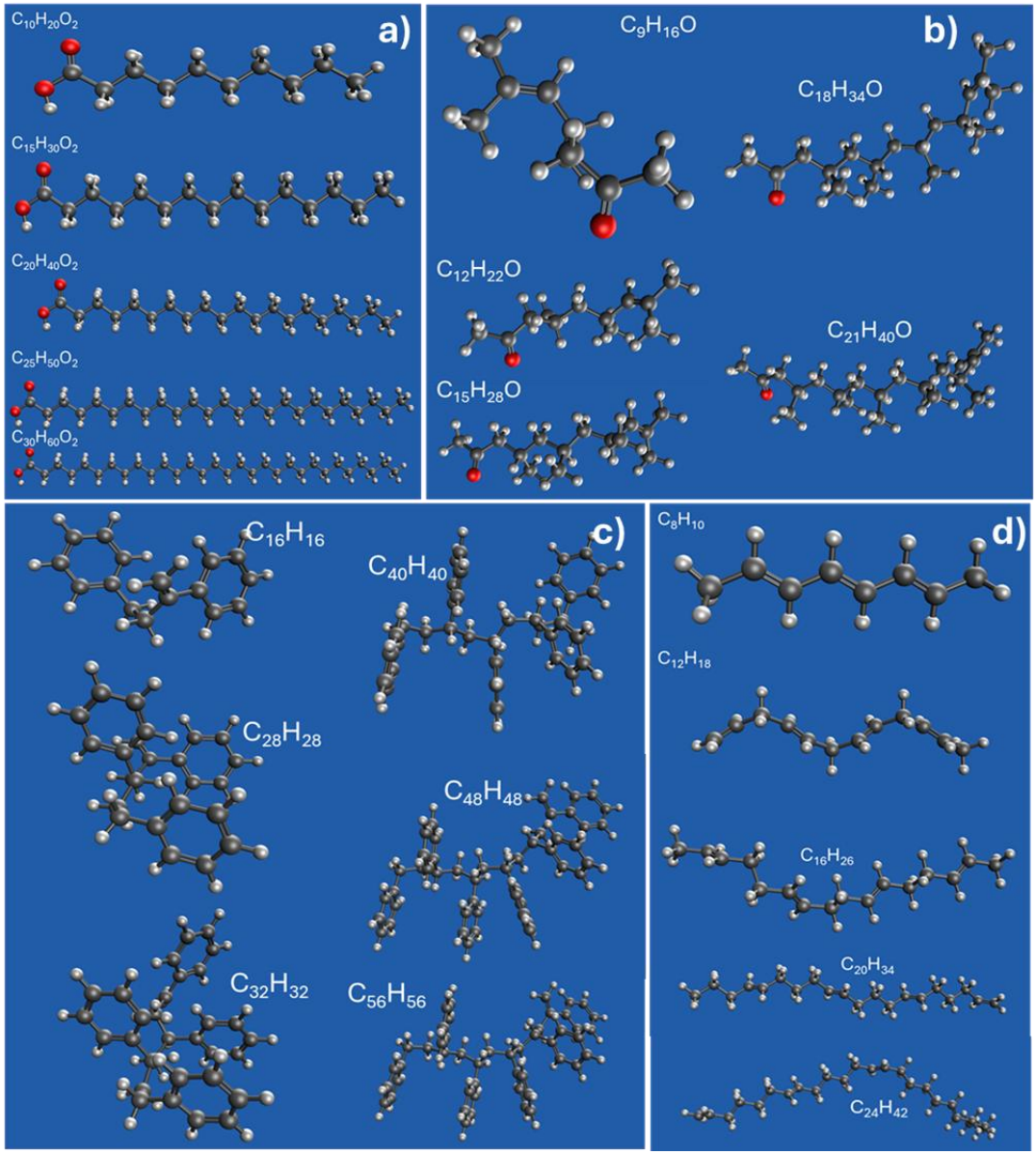

Figure S5. Optimized molecular geometries of selected representative monomerically related thermal decomposition products of (a) PE, (b) PP, (c) PS, and (d) PVC, consisting of several structurally similar homologous species that reflect the original polymer backbone with progressively increasing carbon chain length. The molecular geometries of these compounds were optimized using density functional theory (DFT) with the B3LYP functional and the 6-31G* basis set, enabling estimation of their gas-phase CCS values.

Table S1. Formulas, molecular weights, and collisional cross sections of selected plastic products were determined through computational geometric optimization.

	Representative homologous PE products					
Formula MW (amu)	$C_{10}H_{20}O_2$ 172	$C_{15}H_{30}O_2$ 242	$C_{20}H_{40}O_2$ 312	$C_{25}H_{50}O_2$ 382	$C_{30}H_{60}O_2$ 452	
CCS ($Å^2$)	99.6	134.9	170.4	206.0	241.6	
	Representative homologous PP products					
Formula MW (amu)	$C_8H_{14}O$ 128	$C_{14}H_{26}O$ 212	$C_{20}H_{38}O$ 296	$C_{26}H_{50}O$ 380	$C_{32}H_{26}O$ 464	
CCS ($Å^2$)	81.4	123.6	166.0	208.2	250.6	
	Representative homologous PS products					
Formula MW (amu)	C_8H_8 104	$C_{16}H_{16}$ 208	$C_{24}H_{24}$ 312	$C_{32}H_{32}$ 416	$C_{40}H_{40}$ 520	$C_{48}H_{48}$ 624
CCS ($Å^2$)	63.7	96.9	123.4	148.3	176.3	205.1
	Representative homologous PVC products					
Formula MW (amu)	C_8H_{10} 108	$C_{12}H_{18}$ 162	$C_{16}H_{26}$ 218	$C_{20}H_{34}$ 274	$C_{24}H_{42}$ 330	
CCS ($Å^2$)	76.6	102.2	129.8	157.9	183.3	

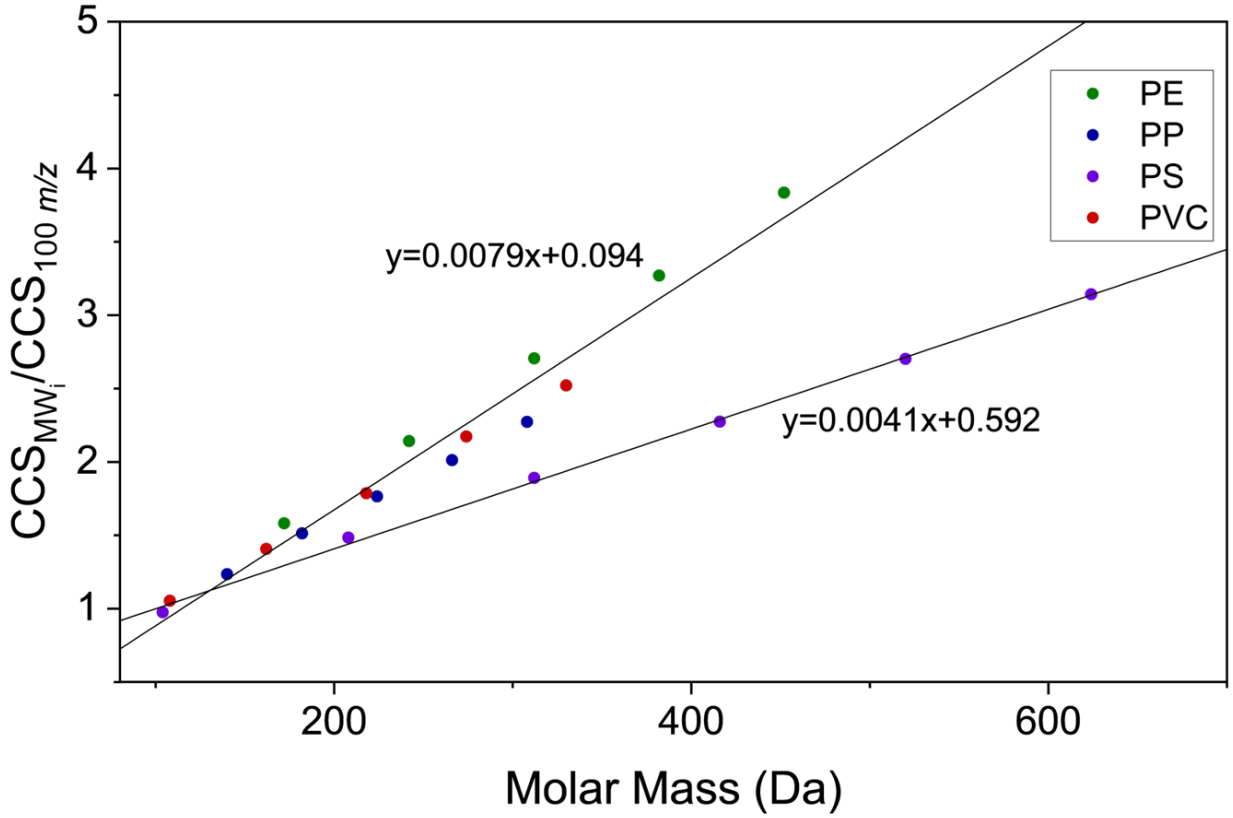

Figure S6. Computationally determined R=CCS$_{MWi}$/CCS$_{100}$ ratios for representative species from the thermal decomposition of four plastic types. These values were used to estimate sensitivity factors (σ_i) applied in Equations 4 and 5 of the main manuscript. A single linear regression fit is applied to data for PE, PP, and PVC products, while a separate regression is used for PS products due to their distinct structural characteristics.

Supplemental Note 3. Parameterization-Based Estimation of Apparent Enthalpies ($^{i}\Delta H^{*}$, kJ mol^{-1}) and Temperature-dependent Saturation Mass Concentrations ($^{i}C^{*}_{T}$, μg·m^{-3}) for Particle-to-Gas Phase Transitions of Plastic Thermal Decomposition Products.

Initial values of saturation mass concentrations at 298K $\log {}^{i}C^{o}_{298K}$ of identified thermal decomposition species were calculated using the 'Molecular Corridors (MC)' parameterization method by Li et al., employing equation S1:

$$logC^{o}{}_{298K} = (n_C^0 - n_C)b_C - n_O b_O - 2\frac{n_C n_O}{n_C + n_O} b_{CO} - n_N b_N - n_S b_S \qquad \text{Eq. S1}$$

where n_C, n_H, and n_O correspond to the number of C, H, and O atoms in individual species. Reference parameters of n_C^0, b_C, b_O, b_N, and b_S were obtained from Table 1 in (Li et al. 2016)

Obtained values of $\log {}^{i}C^{o}_{298K}$ are then refined to yield more accurate values of $\log {}^{i}C^{*}_{298K}$ by applying a correction factor defined by equation S2 derived from comparisons between MC-predicted and experimental volatility data reported for laboratory-generated secondary organic aerosol (SOA) (West et al. 2023), as illustrated in Figure S11.

$$logC^{*}_{298K} = 1.05 * logC^{o}_{298K} - 1.84 \qquad \text{Eq. S2}$$

Figure S7 summarizes $\log {}^{i}C^{*}_{298K}$ values derived for thermal decomposition products of four plastic types.

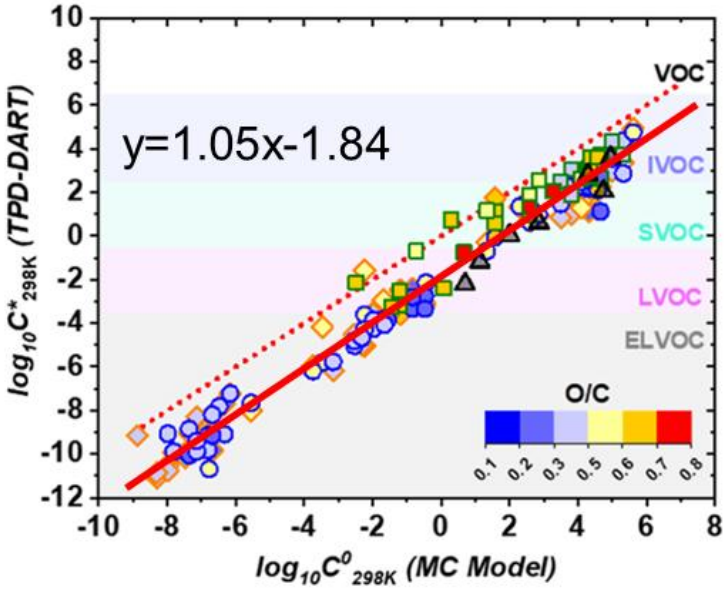

Figure S7. Correlation of experimentally determined ($\log {}^{i}C^{*}_{298K}$) and MC-calculated ($\log {}^{i}C^{*}_{298K}$) values of saturation mass concentrations. Adopted from (West et al. 2023), with permission from the American Chemical Society, copyright 2023.

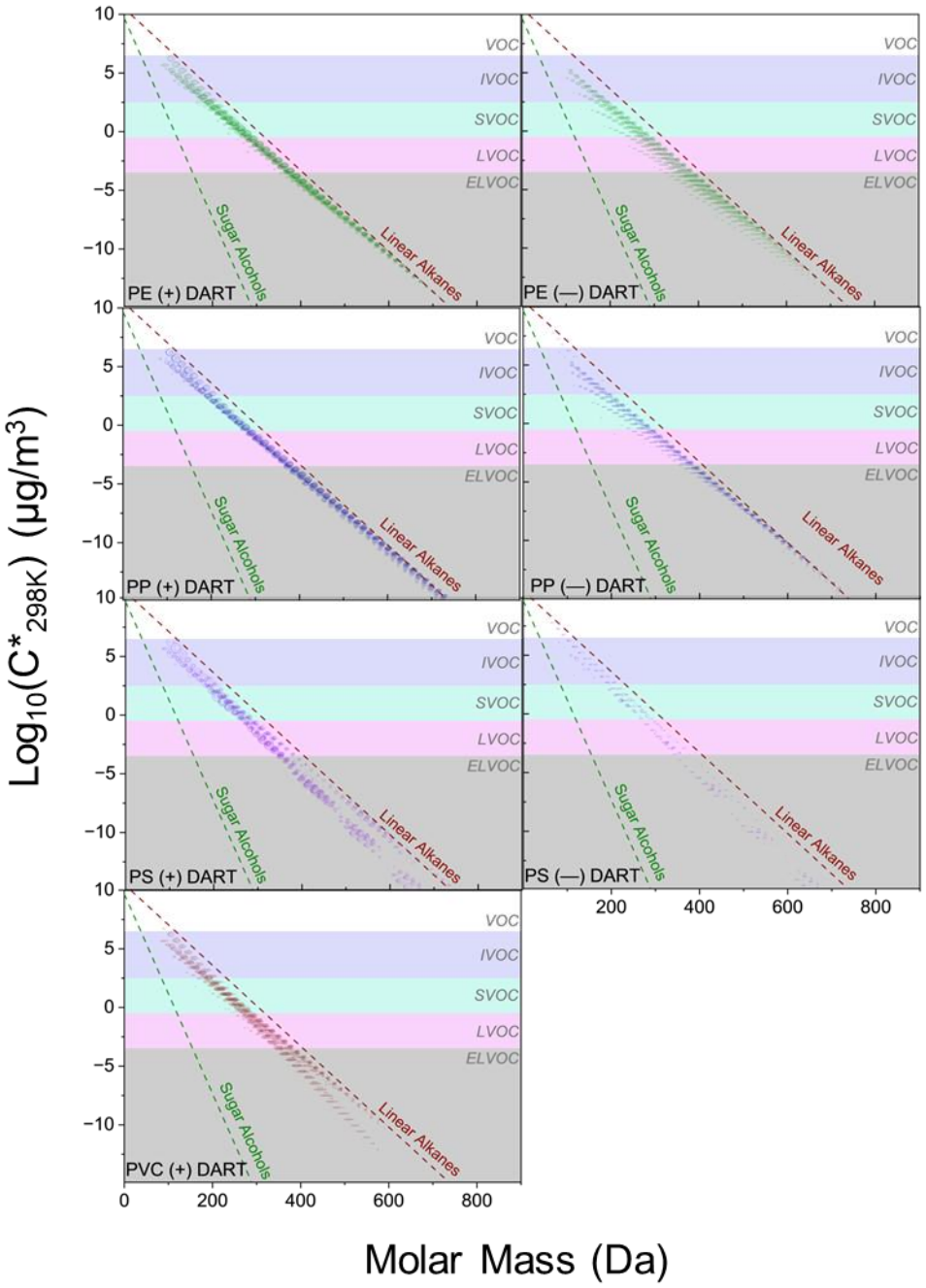

Figure S8. Molecular corridor plots, corrected with correlation line from Figure S7, of the plastic thermal decomposition products detected in positive (left panels) and negative (right panels) modes of TPD-DART-HRMS experiments with PE, PP, PS, and PVC plastic types, Plastic thermal decomposition emissions exhibit a wide range of volatility values from VOC to ELVOC; all detected species are substantially saturated with low degree of aromaticity as indicated by their proximity to the linear alkanes reference line.

The apparent enthalpies of vaporization, ${}^{i}\Delta H^{*}$, for particle-to-gas phase transitions of individual species (i) are calculated from their estimated $\log {}^{i}C^{*}_{298K}$ values using using the parameterization $\Delta H^{*} = -11 \times \log({}^{i}C^{*}_{298K}) + 85$ (Ranjan et al. 2012), which is consistent with experimentally reported values for components of ambient organic aerosol influenced by biomass burning emissions, as shown in Figure S13.

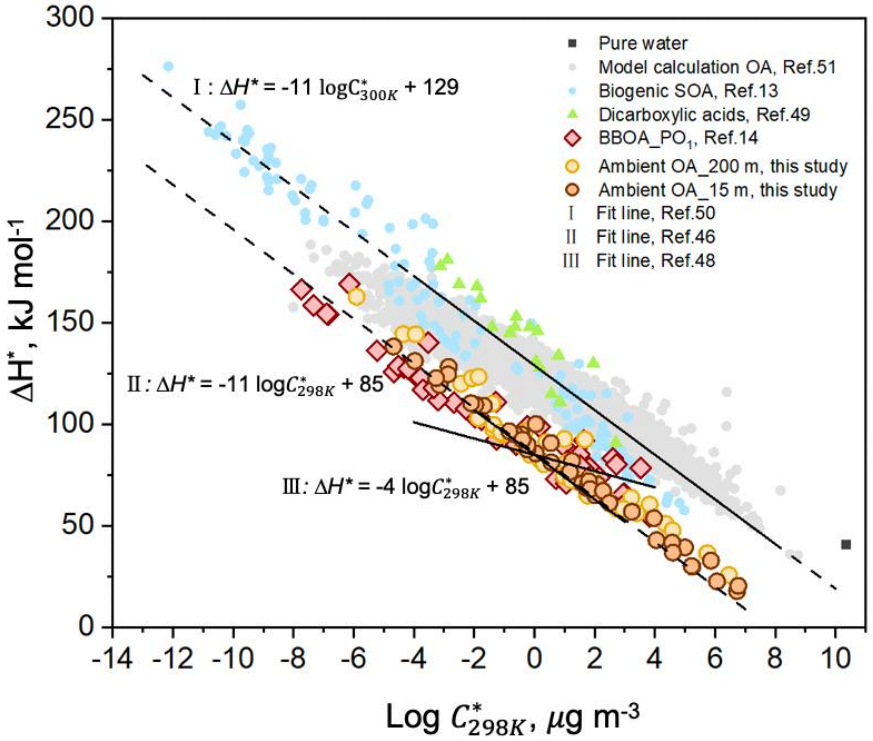

Figure S9. Relationship between apparent enthalpy of condensed-phase to gas-phase transition (${}^{i}\Delta H^{*}$) and $\log {}^{i}c^{*}_{298K}$ for individual species in ambient organic aerosol mixtures, as reported by Xie et al. (2025), and compared with relevant reference parameterizations. All annotations shown are original to the Xie et al. (2025) publication. Fit lines I, II, and III correspond to biogenic SOA, anthropogenic OA, and BBOA, respectively, as proposed by (Epstein et al. 2010), (Ranjan et al. 2012), and (May et al. 2013). Reproduced from Xie et al. (2025) with permission from the American Chemical Society, copyright 2025.

Supplemental Note 4. Volatility and Gas-Particle Partitioning of Plastic Thermal Decomposition Products.

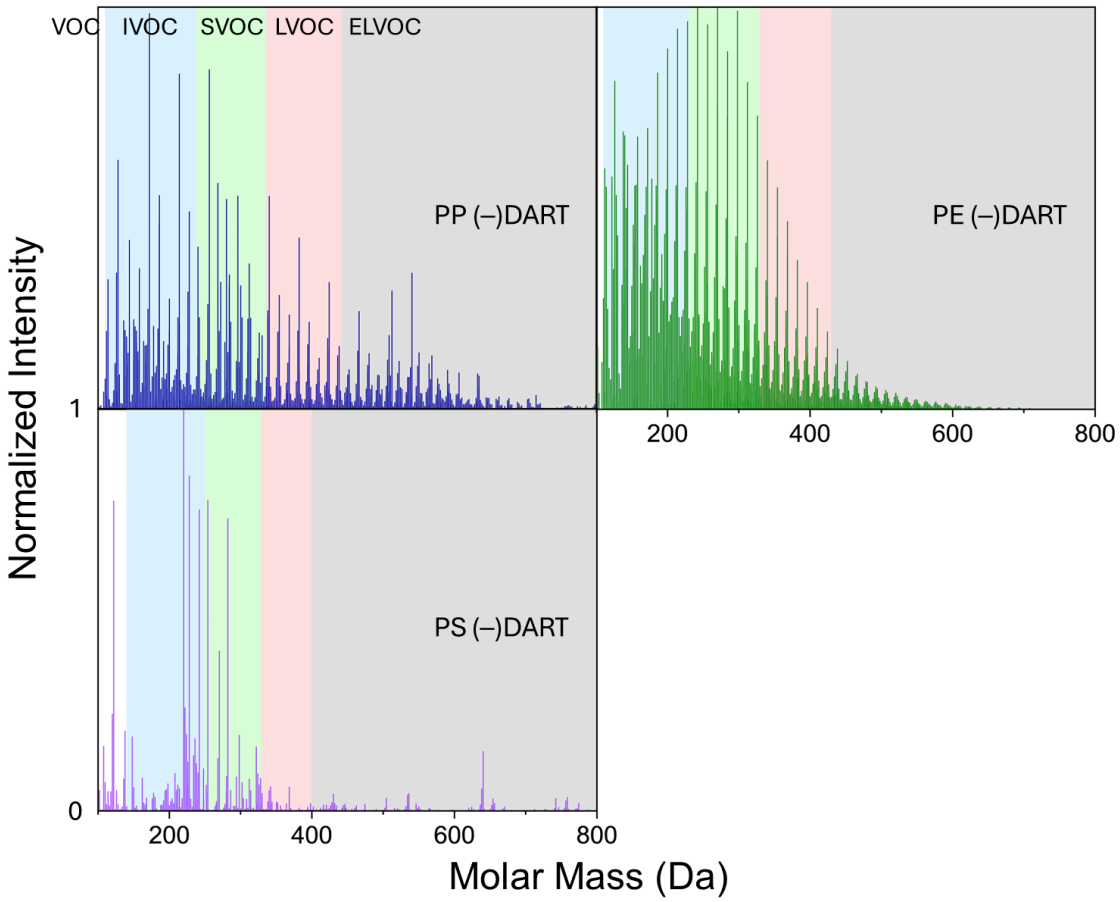

Figure S10. Mass spectra of thermal decomposition products obtained in TPD-(–)DART-HRMS experiments with common plastic types: polypropylene (PP), polyethylene (PE), polystyrene (PS). The background colored regions correspond to volatility classes: volatile organic compounds (VOC), intermediately volatile organic compounds (IVOC), semi-volatile organic compounds (SVOC), low volatile organic compounds (LVOC), and extremely low volatility organic compounds (ELVOC).

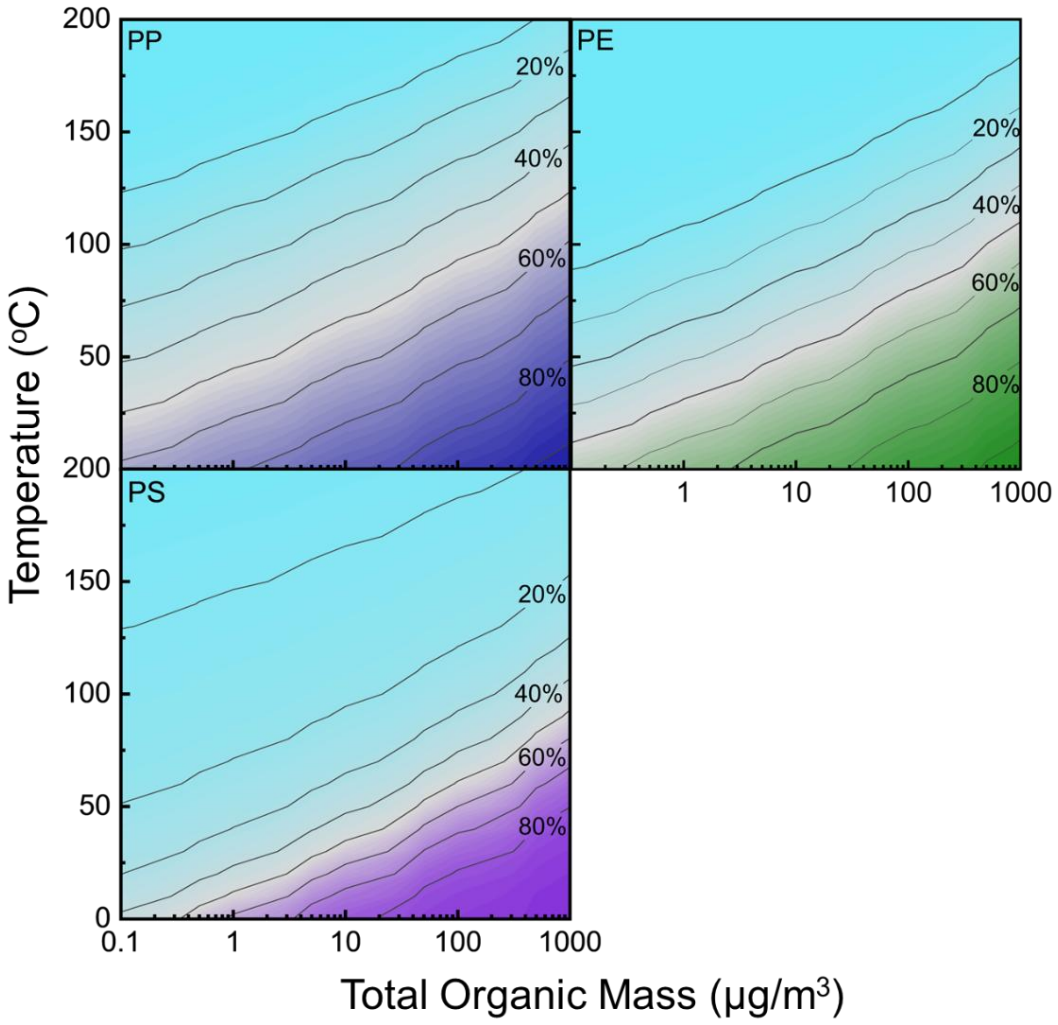

Figure S11. 2D gas-particle partitioning maps for thermal decomposition products of plastic types (PE, PP, PS) calculated from VBS distributions derived using TPD-(−)DART-HRMS experiments. Each map depicts the equilibrium partitioning behavior of plastic-derived products across a broad range of ambient temperatures (T) and total organic mass (C_{tOM}) loadings, illustrating the relative propensity of each plastic's pyrolysis products to exist in the particle versus gas phase under atmospherically relevant conditions. The condensability of the mixtures displayed here is comparable to that detected in positive mode in Figure 4.

Table S2. Values of the total organic mass loadings ($C_{tOM,}$ μg/m^3) and temperatures (ºC) at trajectory points 1-9 are shown in Figures 5 and 6.

Points	**Temperature (K)**	**Mass loading (μg/m^3)**
1	450	700
2	415	400
3	380	250
4	345	150
5	310	100
6	300	25
7	295	6
8	290	1.5
9	285	0.2

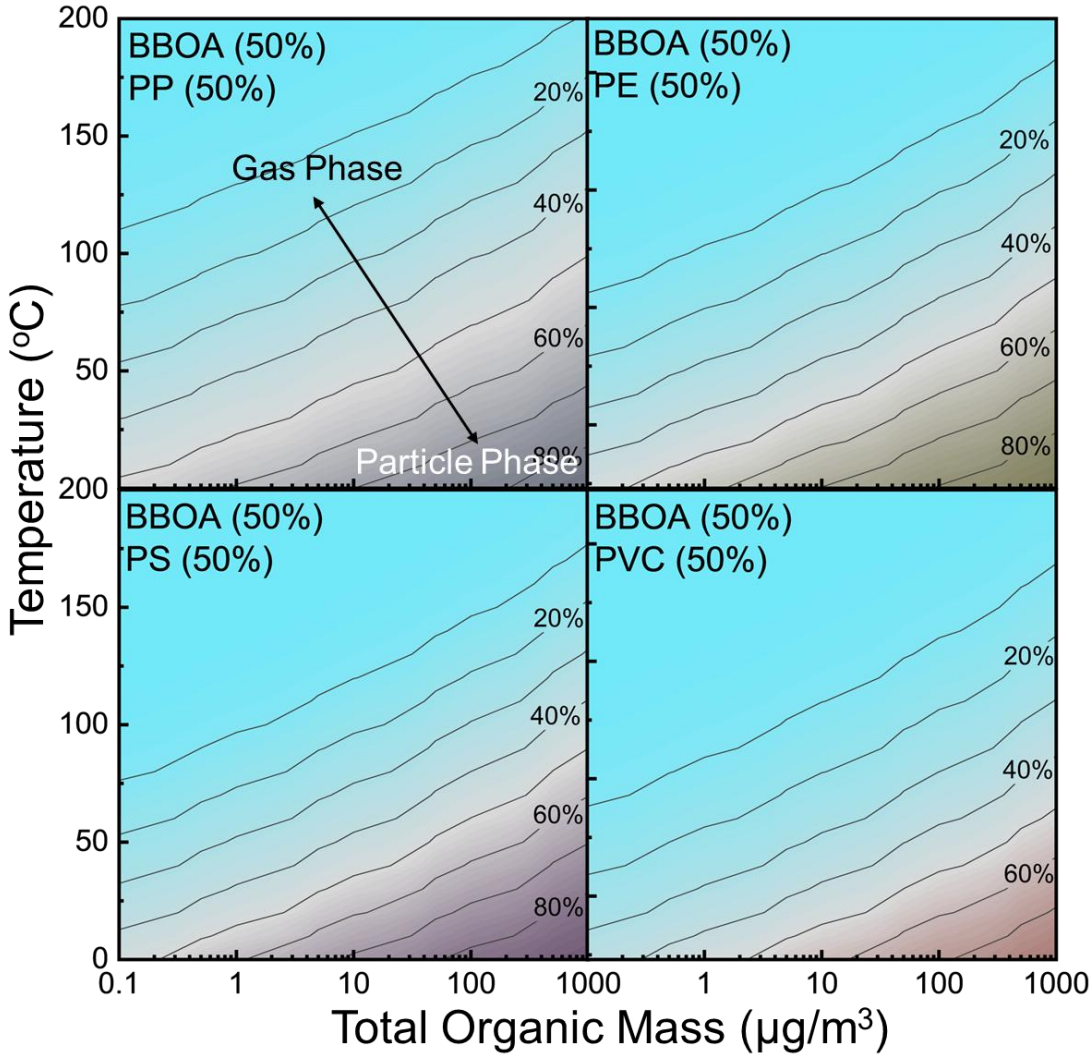

Figure S12. TPD-DART 2D maps of PE, PP, PS, and PVC thermal decomposition products combined with BBOA with a 50%/50% mixing ratio by mass. Each map depicts the equilibrium partitioning behavior of composite products across a broad range of ambient temperatures (T) and total organic mass (C_{tOM}) loadings, illustrating the relative propensity of each mixture to exist in the particle versus gas phase under atmospherically relevant conditions.

Supplemental Note 5. Parameterization-Based Viscosity Estimation for Plastic Thermal Decomposition Products and their Condensed-Phase Mixtures.

Glass transition temperatures T_g of plastic thermal decomposition species were calculated following DeRieux et. al. using equation S3:

$$T_g = \left(n_C^0 + \ln(n_C)\right)b_C + \ln(n_H)\, b_H + \ln(n_C)\ln(n_H)\, b_{CH} + \ln(n_O)\, b_O + \ln(n_C)\ln(n_O) b_{CO} \quad \text{Eq. S3}$$

Reference parameters for n_C^0 (reference carbon number) and b values (atomic contributions to T_g) are obtained from Table 1 in (DeRieux et al. 2018). Vogel temperatures of the plastic thermal decomposition species were calculated using equation S4. D is the fragility parameter assumed to be 10 for organic compounds.(DeRieux et al. 2018)

$$T_0 = \frac{39.17 T_g}{D+39.17} \quad \text{Eq. S4}$$

Viscosity parameters (η) of the plastic thermal decomposition species were calculated with equation S5. T_g and T_0 are obtained from equations S3 and S4, respectively. D is the fragility parameter assumed to be 10 for organic compounds.(DeRieux et al. 2018)

$$log\ \eta = -5 + 0.434 \frac{T_0 D}{T_g - T_0} \quad \text{Eq. S5}$$

From this method, viscosity values are estimated for individual components of a mixture. To extend this framework to estimate the viscosity of bulk aerosol samples, the glass transition temperature of an organic mixture is estimated as follows, where ω_i is the mass fraction of each component (i):

$$T_{g,org} = \sum_i \ \omega_i T_{g,i} \quad \text{Eq. S6}$$

For an aerosol at a specific relative humidity, ω_{org} is the fraction of organic material in the condensed phase, or ω_{org}=$mass_{org}$/($mass_{org}$+$mass_{water}$) (Xie et al. 2024). To estimate the equilibrium of organic/water mixtures from Kohler theory, we need to establish a hygroscopicity parameter κ for plastic thermal decomposition samples. Here, we apply a κ value of 0.1 in Figures 8, S17, and S18, while showing calculation results with different κ values of 0.02 and 0.05 in Figures S19-S20.

For an aerosol/water mixture at a certain relative humidity, the Gordon-Taylor equation can be applied to determine the bulk glass transition temperature, where $T_{g,w,}$ and k_{GT} are the glass transition temperature of pure water and the Gordon-Taylor constant.

$$T_g\left(\omega_{org,RH}\right) = \frac{(1-\omega_{org,RH})T_{g,w} + \frac{1}{k_{GT}}\omega_{org,RH}T_{g,org}}{(1-\omega_{org,RH}) + \frac{1}{k_{GT}}\omega_{org,RH}} \quad \text{Eq. S7}$$

The viscosity of this bulk aerosol mixture can be determined from the equations outlined in equations S4 and S5.

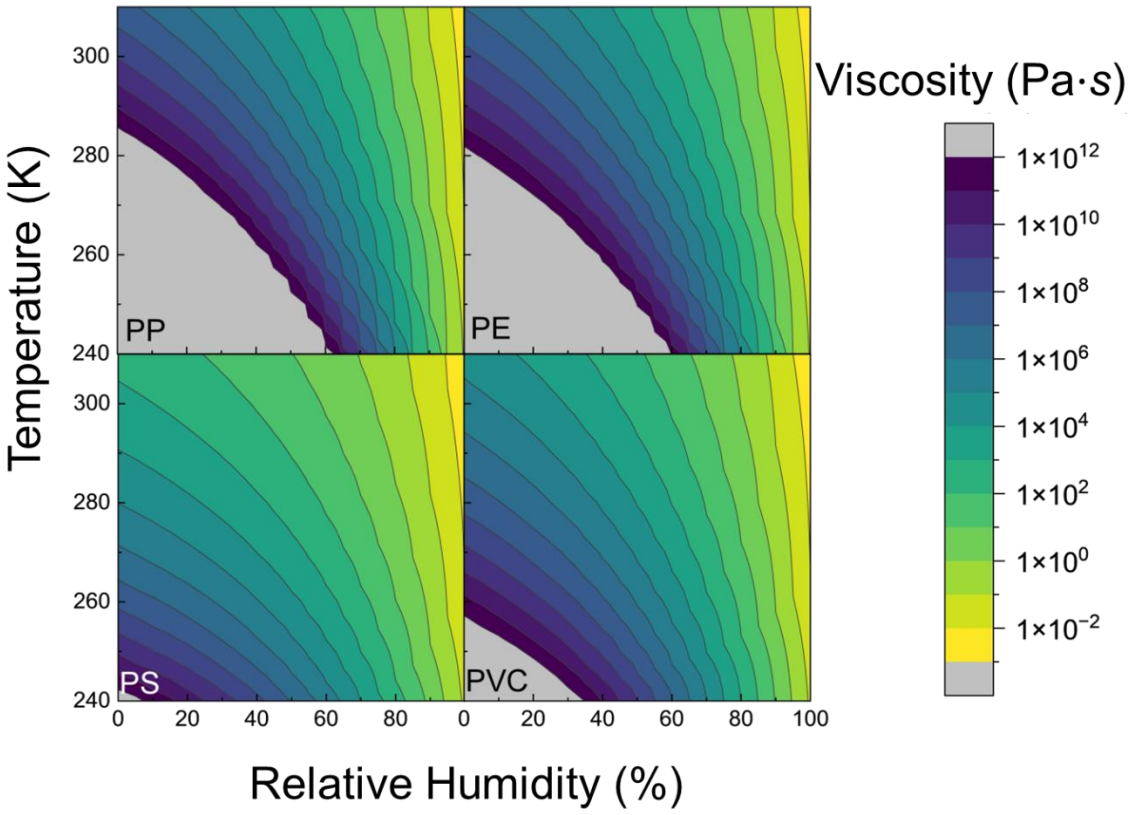

Figure S13. Viscosity maps for mixtures of thermal decomposition products of four plastic types (PE, PP, PS, and PVC) calculated from VBS distributions derived from TPD-(+)DART-HRMS experiments. Each map depicts the viscosity values of condensed-phase mixtures calculated across a range of ambient temperatures (T) and relative humidity, assuming mass loading conditions of C_{tOM} =100 μg/m^3. PVC and PS are estimated to be much less viscous than PE and PP at similar relative humidity and temperature values.

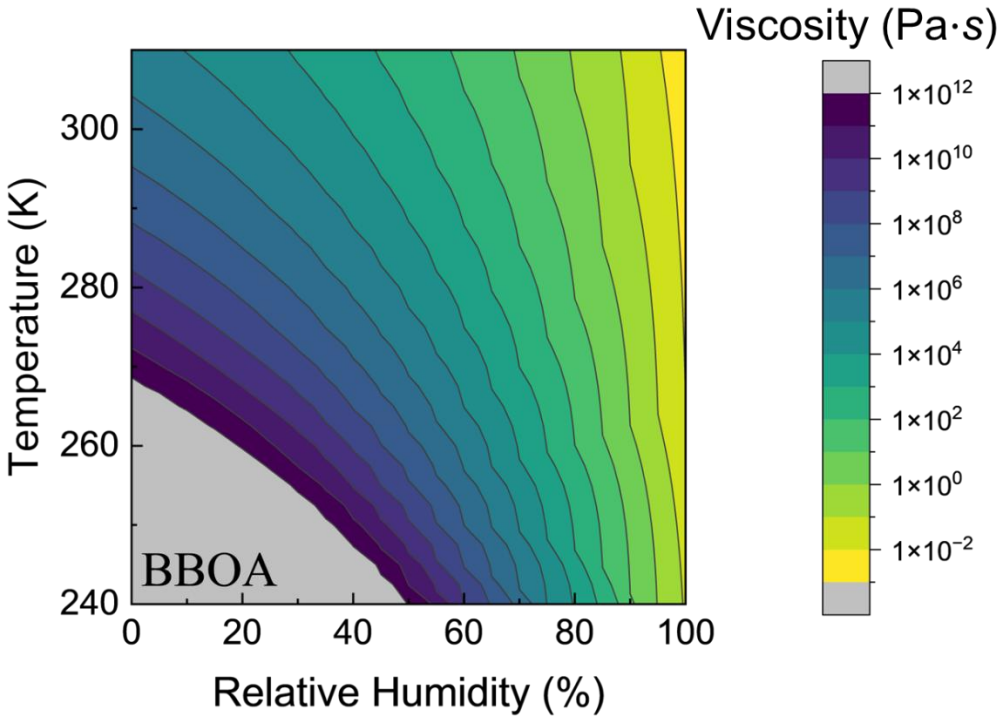

Figure S14. Viscosity maps for mixtures of biomass burning calculated from VBS distributions derived from TPD-(—)DART-HRMS experiments. Each map depicts the viscosity values of condensed-phase mixtures calculated across a range of ambient temperatures (T) and relative humidity, assuming mass loading conditions of C_{tOM} =100 μg/m^3.

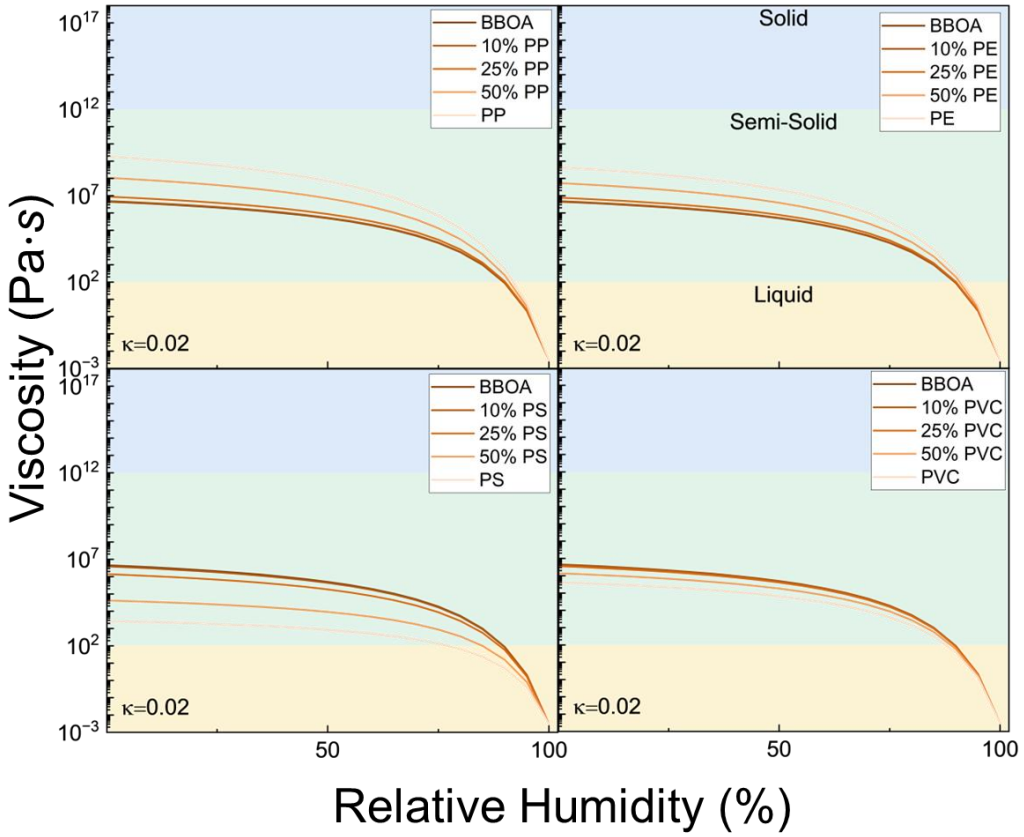

Figure S15. Viscosity of composite particles composed of BBOA and plastic thermal decomposition products derived from four plastic types (PP, PE, PS, and PVC) at mixing ratios of 0% (all BBOA), 10%, 25%, 50%, and 100% (all plastic-derived products). Viscosity values at dry conditions (0% RH) were calculated under conditions of C_{tOM} =100 μg/m^3 and 25 °C. Humidity-dependent values were calculated assuming a hygroscopicity parameter κ=0.02. Additional plots assuming different κ values of 0.05 and 0.1 are provided in Figures 8 and S16.

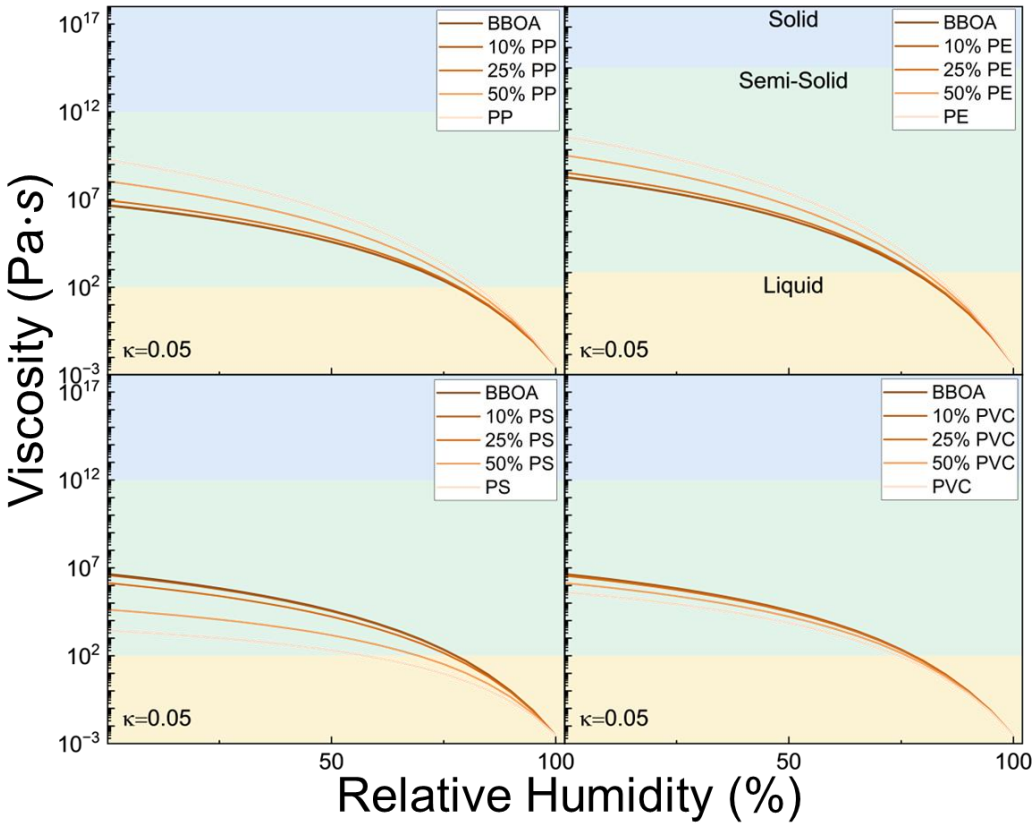

Figure S16. Viscosity of composite particles composed of BBOA and plastic thermal decomposition products derived from four plastic types (PP, PE, PS, and PVC) at mixing ratios of 0% (all BBOA), 10%, 25%, 50%, and 100% (all plastic-derived products). Viscosity values at dry conditions (0% RH) were calculated under conditions of C_{tOM} =100 μg/m^3 and 25 °C. Humidity-dependent values were calculated assuming a hygroscopicity parameter κ=0.05. Additional plots, assuming different κ values of 0.02 and 0.1, are provided in Figures 8 and S15.

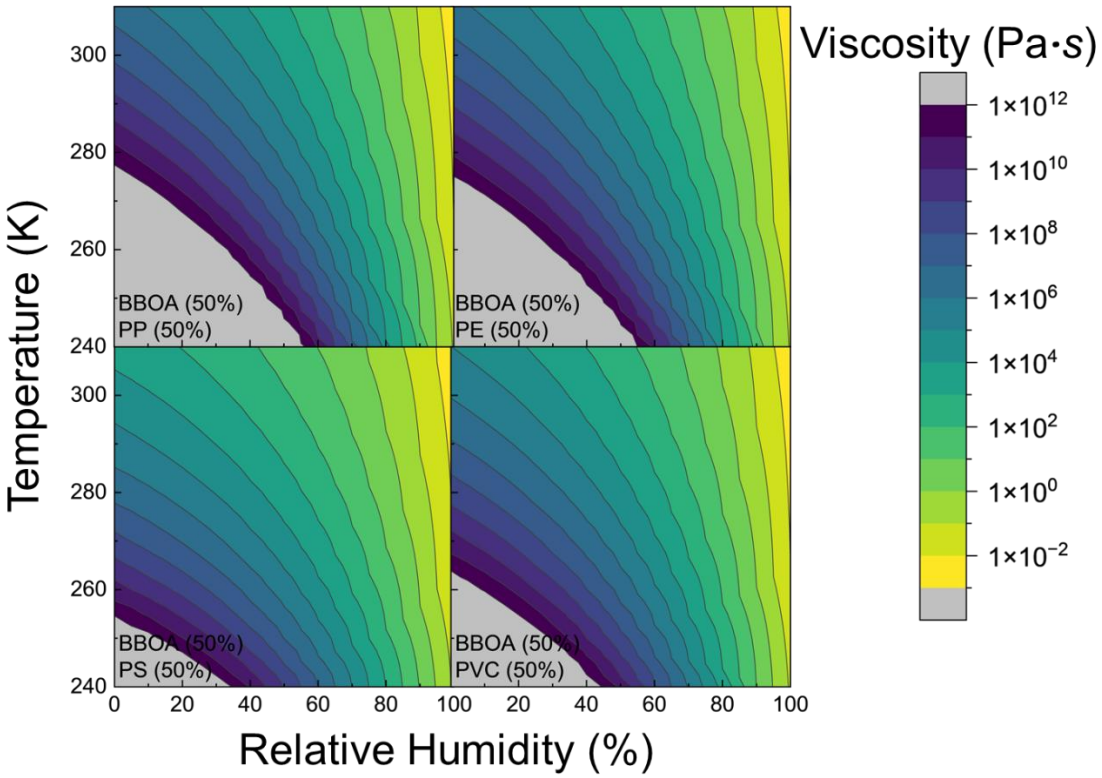

Figure S17. Viscosity maps for composite particles composed of BBOA and plastic thermal decomposition products derived from four plastic types (PP, PE, PS, and PVC) calculated from VBS distributions derived from TPD-(+)DART-HRMS experiments. Each map depicts the viscosity values of condensed-phase mixtures calculated across a range of ambient temperatures (T) and relative humidity, assuming mass loading conditions of C_{tOM} =100 μg/m^3.

Supplemental Note 6. Parameterization-Based Estimation of Particle-to-Gas Phase Transitions of Plastic Thermal Decomposition Products and Biomass Burning Mixes using high-volatility estimate.

The plots in Figure S18-S20 were constructed with the volatility limit I $\Delta H^* = -11\times\log(C^*_{298K}) + 129$ (Epstein et al. 2010), resulting in less condensable aerosol for both plastic thermal decomposition products and mixed BBOA and plastic thermal decomposition aerosol.

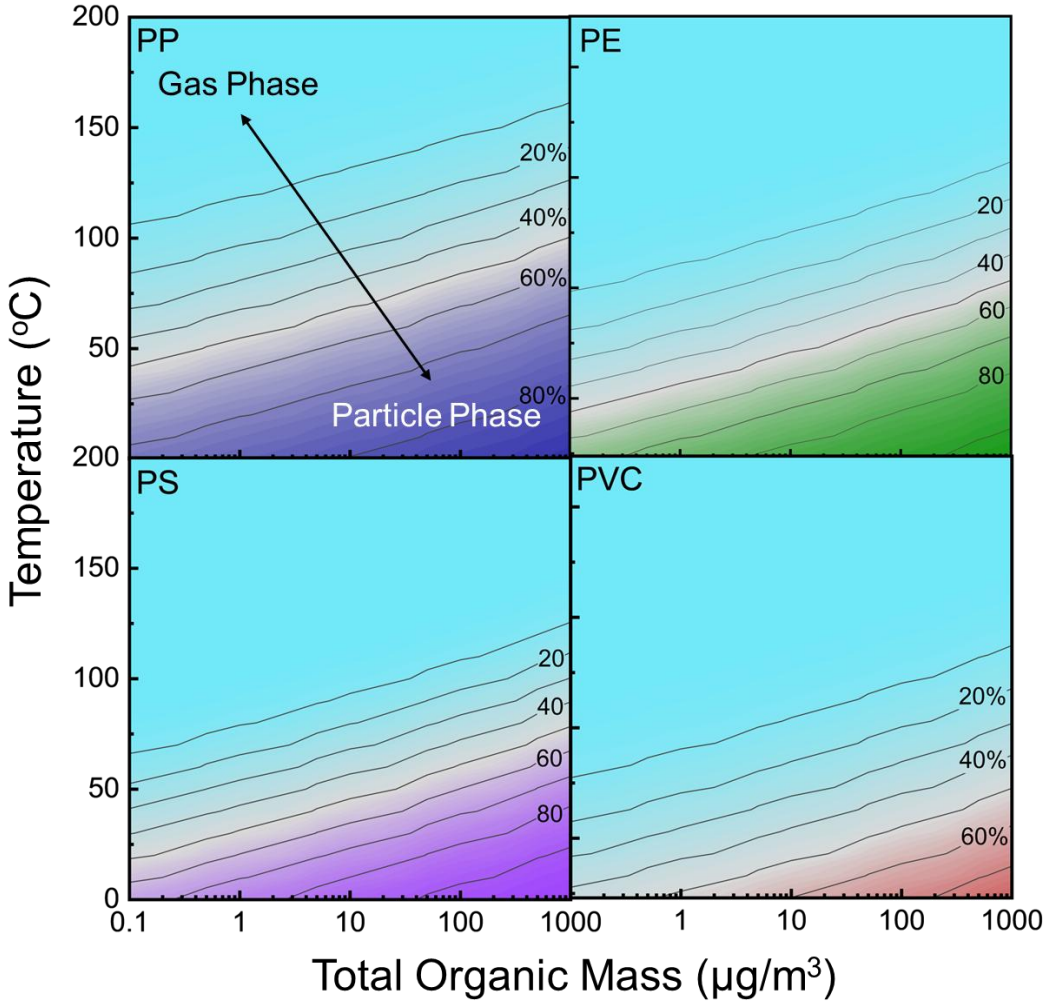

Figure S18. 2D gas-particle partitioning maps for thermal decomposition products of four plastic types (PE, PP, PS, and PVC) calculated from VBS distributions derived using TPD-(+)DART-HRMS experiments. Each map depicts the equilibrium partitioning behavior of plastic-derived products across a broad range of ambient temperatures (T) and total organic mass (C_{tOM}) loadings, illustrating the relative propensity of each plastic's pyrolysis products to exist in the particle versus gas phase under atmospherically relevant conditions. These calculations are determined from the high volatility correlation of ΔH* and logC^*_{298K} compared with the low volatility estimate in Figure 5.

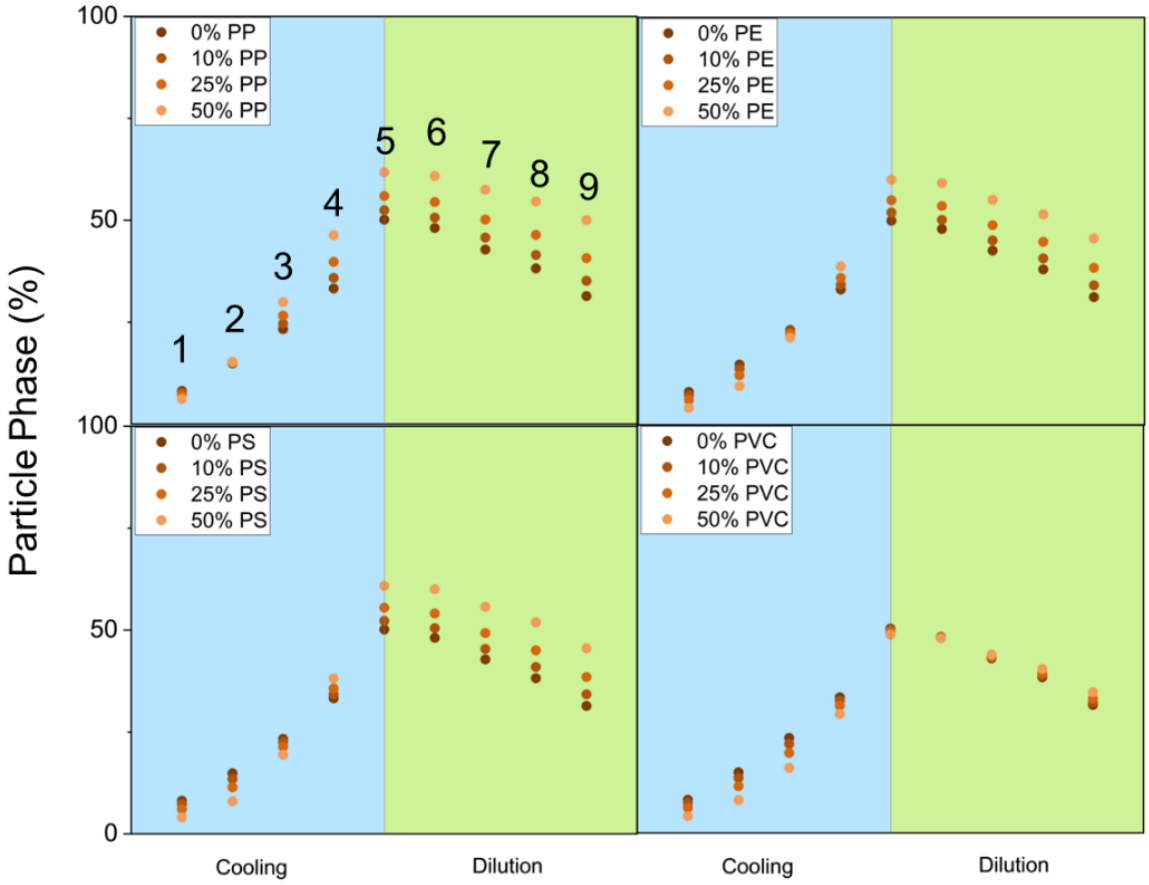

Figure S19. Particle-phase fractions of mixed emissions composed of BBOA and thermal decomposition products derived from four plastic types (PP, PE, PS, and PVC) at mixing ratios of 0% (all BBOA), 10%, 25%, and 50%. Calculations are performed for T and C_{tOM} conditions corresponding to trajectory points 1–9, as depicted in Figure 6, illustrating an example of emissions evolution through cooling (points 1–5) and dilution (points 5–9) as the plume disperses from the source. These calculations are determined from the high volatility correlation of ΔH* and log$C^*_{298K,}$ comparable with the low volatility estimate in Figure 7.

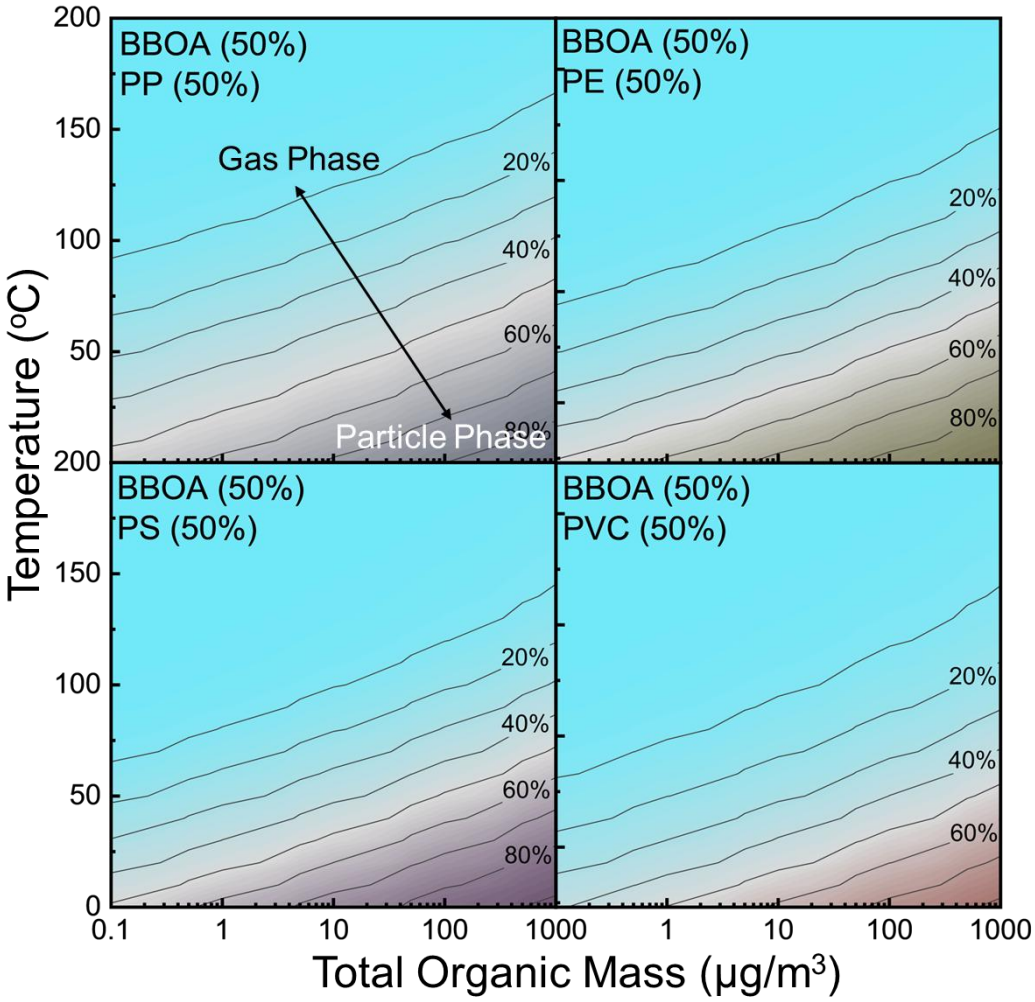

Figure S20. TPD-DART 2D maps of PE, PP, PS, and PVC thermal decomposition products combined with BBOA with a 50%/50% mixing ratio by mass. Each map depicts the equilibrium partitioning behavior of composite products across a broad range of ambient temperatures (T) and total organic mass (C_{tOM}) loadings, illustrating the relative propensity of each mixture to exist in the particle versus gas phase under atmospherically relevant conditions. These calculations are determined from the high volatility correlation of ΔH^* and $\log C^*_{298K,}$ comparable with the low volatility estimate in Figure S12.

References

Donahue, N.M., Kroll, J.H., Pandis, S.N., and Robinson, A.L. (2012). A two-dimensional volatility basis set – Part 2: Diagnostics of organic-aerosol evolution. *Atmos. Chem. Phys.* 12 (2):615–634. doi:10.5194/acp-12-615-2012.

Epifanovsky, E., Gilbert, A.T.B., Feng, X., Lee, J., Mao, Y., Mardirossian, N., Pokhilko, P., White, A.F., Coons, M.P., Dempwolff, A.L., Gan, Z., Hait, D., Horn, P.R., Jacobson, L.D., Kaliman, I., Kussmann, J., Lange, A.W., Lao, K.U., Levine, D.S., Liu, J., McKenzie, S.C., Morrison, A.F., Nanda, K.D., Plasser, F., Rehn, D.R., Vidal, M.L., You, Z.-Q., Zhu, Y., Alam, B., Albrecht, B.J., Aldossary, A., Alguire, E., Andersen, J.H., Athavale, V., Barton, D., Begam, K., Behn, A., Bellonzi, N., Bernard, Y.A., Berquist, E.J., Burton, H.G.A., Carreras, A., Carter-Fenk, K., Chakraborty, R., Chien, A.D., Closser, K.D., Cofer-Shabica, V., Dasgupta, S., de Wergifosse, M., Deng, J., Diedenhofen, M., Do, H., Ehlert, S., Fang, P.-T., Fatehi, S., Feng, Q., Friedhoff, T., Gayvert, J., Ge, Q., Gidofalvi, G., Goldey, M., Gomes, J., González-Espinoza, C.E., Gulania, S., Gunina, A.O., Hanson-Heine, M.W.D., Harbach, P.H.P., Hauser, A., Herbst, M.F., Hernández Vera, M., Hodecker, M., Holden, Z.C., Houck, S., Huang, X., Hui, K., Huynh, B.C., Ivanov, M., Jász, Á., Ji, H., Jiang, H., Kaduk, B., Kähler, S., Khistyaev, K., Kim, J., Kis, G., Klunzinger, P., Koczor-Benda, Z., Koh, J.H., Kosenkov, D., Koulias, L., Kowalczyk, T., Krauter, C.M., Kue, K., Kunitsa, A., Kus, T., Ladjánszki, I., Landau, A., Lawler, K.V., Lefrancois, D., Lehtola, S., Li, R.R., Li, Y.-P., Liang, J., Liebenthal, M., Lin, H.-H., Lin, Y.-S., Liu, F., Liu, K.-Y., Loipersberger, M., Luenser, A., Manjanath, A., Manohar, P., Mansoor, E., Manzer, S.F., Mao, S.-P., Marenich, A.V., Markovich, T., Mason, S., Maurer, S.A., McLaughlin, P.F., Menger, M.F.S.J., Mewes, J.-M., Mewes, S.A., Morgante, P., Mullinax, J.W., Oosterbaan, K.J., Paran, G., Paul, A.C., Paul, S.K., Pavošević, F., Pei, Z., Prager, S., Proynov, E.I., Rák, Á., Ramos-Cordoba, E., Rana, B., Rask, A.E., Rettig, A., Richard, R.M., Rob, F., Rossomme, E., Scheele, T., Scheurer, M., Schneider, M., Sergueev, N., Sharada, S.M., Skomorowski, W., Small, D.W., Stein, C.J., Su, Y.-C., Sundstrom, E.J., Tao, Z., Thirman, J., Tornai, G.J., Tsuchimochi, T., Tubman, N.M., Veccham, S.P., Vydrov, O., Wenzel, J., Witte, J., Yamada, A., Yao, K., Yeganeh, S., Yost, S.R., Zech, A., Zhang, I.Y., Zhang, X., Zhang, Y., Zuev, D., Aspuru-Guzik, A., Bell, A.T., Besley, N.A., Bravaya, K.B., Brooks, B.R., Casanova, D., Chai, J.-D., Coriani, S., Cramer, C.J., Cserey, G., DePrince, A.E., III, DiStasio, R.A., Jr., Dreuw, A., Dunietz, B.D., Furlani, T.R., Goddard, W.A., III, Hammes-Schiffer, S., Head-Gordon, T., Hehre, W.J., Hsu, C.-P., Jagau, T.-C., Jung, Y., Klamt, A., Kong, J., Lambrecht, D.S., Liang, W., Mayhall, N.J., McCurdy, C.W., Neaton, J.B., Ochsenfeld, C., Parkhill, J.A., Peverati, R., Rassolov, V.A., Shao, Y., Slipchenko, L.V., Stauch, T., Steele, R.P., Subotnik, J.E., Thom, A.J.W., Tkatchenko, A., Truhlar, D.G., Van Voorhis, T., Wesolowski, T.A., Whaley, K.B., Woodcock, H.L., III, Zimmerman, P.M., Faraji, S., Gill, P.M.W., Head-Gordon, M., Herbert, J.M., and Krylov, A.I. (2021). Software for the frontiers of quantum chemistry: An overview of developments in the Q-Chem 5 package. *The Journal of Chemical Physics* 155 (8):084801. doi:10.1063/5.0055522.

Epstein, S.A., Riipinen, I., and Donahue, N.M. (2010). A Semiempirical Correlation between Enthalpy of Vaporization and Saturation Concentration for Organic Aerosol. *Environ. Sci. Technol.* 44 (2):743–748. doi:10.1021/es902497z.

Halpern, E., Heirty, L., West, C., Li, Y., Kim, W.M., Mennito, A.S., and Laskin, A. (2025). Chemical characterization of polymer and chloride content in waste plastic materials

using pyrolysis – direct analysis in real time – high-resolution mass spectrometry. *Environ. Sci.: Processes Impacts* 27 (1):104–118. doi:10.1039/D4EM00501E.

May, A.A., Presto, A.A., Hennigan, C.J., Nguyen, N.T., Gordon, T.D., and Robinson, A.L. (2013). Gas-Particle Partitioning of Primary Organic Aerosol Emissions: (2) Diesel Vehicles. *Environ. Sci. Technol.* 47 (15):8288–8296. doi:10.1021/es400782j.

Ranjan, M., Presto, A.A., May, A.A., and Robinson, A.L. (2012). Temperature Dependence of Gas–Particle Partitioning of Primary Organic Aerosol Emissions from a Small Diesel Engine. *Aerosol Science and Technology* 46 (1):13–21. doi:10.1080/02786826.2011.602761.

West, C.P., Hsu, Y.-J., MacFeely, K.T., Huston, S.M., Aridjis-Olivos, B.P., Morales, A.C., and Laskin, A. (2023). Volatility Measurements of Individual Components in Organic Aerosol Mixtures Using Temperature-Programmed Desorption–Direct Analysis in Real Time–High Resolution Mass Spectrometry. *Anal. Chem.* 95 (19):7403–7408. doi:10.1021/acs.analchem.3c00923.

Xie, Q., Gerrebos, N.G.A., Calderon-Arrieta, D., Morton, I.S., Halpern, E.R., Li, C., Zeng, M.F., Bertram, A.K., Rudich, Y., and Laskin, A. (2024). Molecular Insights into Gas–Particle Partitioning and Viscosity of Atmospheric Brown Carbon. *Environ. Sci. Technol.* 58 (41):18284–18294. doi:10.1021/acs.est.4c05650.

Yu, J., Sun, L., Ma, C., Qiao, Y., and Yao, H. (2016). Thermal degradation of PVC: A review. *Waste Management* 48:300–314. doi:10.1016/j.wasman.2015.11.041.